



CALIFORNIA POLYTECHNIC STATE UNIVERSITY

MATERIALS ENGINEERING DEPARTMENT

SENIOR PROJECT REPORT

CHARACTERIZATION OF SLM PRINTED
316L STAINLESS STEEL AND
INVESTIGATION OF MICRO LATTICE
GEOMETRY.

FINLEY MARBURY

JUNE 23, 2017

Contents

Title Page	1
Table of Contents	2
Abstract	3
Acknowledgments	4
1 Introduction	5
Introduction	5
1.1 Cellular Materials	5
1.2 Metal Additive Manufacturing	6
2 Literature Review	9
2.1 Metallic Microlattices	9
2.1.1 Summary	12
2.2 Metallography and Morphology	13
2.3 Qualifying and Characterizing 3D Printed Materials.	14
3 Experimental Procedure	15
3.1 Fabrication of Printed 316L Samples	15
3.1.1 SLM Prints	15
3.1.2 Heat Treatment	17
3.1.3 Machining	17
3.1.4 Lattice Selection	18
3.1.5 Lattice Generation, Printing and Testing	18
3.2 Testing	19
3.2.1 Tension testing	19
3.2.2 Hardness	19
3.2.3 Porosity	20
3.3 Metallography	20
3.3.1 SEM	20
4 Results and Discussion	21

4.1	316L Stainless Steel Characterization	21
4.1.1	Printer Functionality	21
4.1.2	Surface Morphology and Porosity	22
4.1.3	Microstructure	23
4.1.4	Hardness	25
4.1.5	Mechanical Testing	26
4.1.6	XRD Analysis	27
4.1.7	Fracture Images	28
4.1.8	Microlattice Compression Testing	29
5	Conclusions	31
6	Future Work	32
	References	33

Abstract

The goal of this project was firstly to characterize Cal Poly's SLM printed 316L stainless steel. SEM analysis showed Cal Poly's as-printed 316L material to have a cellular dendritic microstructure containing mostly austenite and a small amount of δ -ferrite. After being heat treated to eliminate warp, its yield and ultimate tensile strength were on par with the literature, however higher modulus and lower elongation were observed. XRD analysis confirmed residual stresses in the material, and that grains are preferentially oriented in both heat treated and non heat treated samples. The amount of porosity in the material was found to be about 0.93%, and the material experiences ductile fracture. The second part of the project was to test four different microlattice geometries in uniaxial compression, the octet truss was the most efficient geometry having the highest specific stiffness.

Acknowledgements

This project's completion relied heavily on the help of many Cal Poly students and faculty. I would like to mention a few individuals by name:

- Dr. Kathy Chen - For advising this project and being a mentor to me throughout the process.
- Dr. Wang - For advising this project and accelerating the setup of the SLM printer.
- David Otsu - For being an excellent lab partner and taking ownership for running the SLM.
- Wyatt Hall - For assistance machining tensile samples.
- Stephen Knaus- For providing invaluable technical direction and guidance on microlattices and printing parameters
- Chris Hickok - For providing a copy of the Element nTopology software, making generating the microlattices exponentially easier.
- Lawrence Livermore National Labs - For donating the SLM 125HL printer to Cal Poly.
- Cal Poly Materials Engineering for the use of facilities and guidance through the years.
- Eric Beaton - For keeping all the equipment in the MATE labs running and helping set up the Autodesk Ember.

Chapter 1

Introduction

Cal Poly's Industrial and Manufacturing Engineering department received an SLM 125HL metal 3D printer as a donation from Lawrence Livermore National Labs. The printer uses a process called Selective Laser Melting (SLM) to melt fine metal powder in a bed, layer by layer, until a part is constructed. The SLM process however, is extremely complex and the performance of the material often varies from printer to printer. In order for Cal Poly students to utilize the printer to its full potential, the material, 316L stainless steel must be characterized.

One novel material whose production is enabled by the SLM printing process are metallic microlattices. Microlattice materials are similar to foams in that they have feature sizes on the micron level, the difference is that they are ordered in their structure. Having the knowledge to print effective microlattices here at Cal Poly would give students the ability to make stiff, yet light-weight functional parts.

The following chapter serves as an explanation of why it is valuable to study cellular materials and how the SLM process works.

1.1 Cellular Materials

Nature has developed cellular materials for applications where a high strength to weight ratio is needed. Examples of this can be seen in honeycombs, trabecular bone, and plant stems shown in Figure 1.1. The success of these natural phenomena highlight the importance of studying small scale, optimized, cellular materials. By understanding how nature engineers these materials we can mimic her designs to create our own high strength, low-density materials for use in industries such as aerospace and automotive. Some man-made examples of cellular materials include stochastic foams, regularly ordered lattices and Nomex or aluminum honeycomb cores. Under the category of regularly ordered lattices are microlattices which are sometimes referred to as micro-architected materials. Microlattices are bulk materials made up of smaller, regularly arranged structures with geometries that are generally optimized for given loading conditions. Unlike foams whose members

are organized randomly, microlattices are regular have a repeating pattern or unit cell. Because of this microlattices are theoretically more structurally efficient than foams.

Microlattices have another advantage over foams which is that they are able to be optimized. With advances in modeling and manufacturing every parameter of a lattice material can be tailored for the application, as such, much effort has been put into the design and computational analysis of microlattices. Lastly, because lattices are open-cell they can be used in a number of non-structural applications such as thermal management, filtration, energy absorption and acoustic insulation [1].

Microlattices have been made in a wide variety of materials and processes. Some examples of these processes are bulk photopolymerization, 3D printing methods, and casting. Each method has its limitations but as mentioned previously, metal 3D printing is one method of making microlattices that has grown in popularity because of the ease at which one can print microlattices inside parts for added stiffness with a low weight penalty.

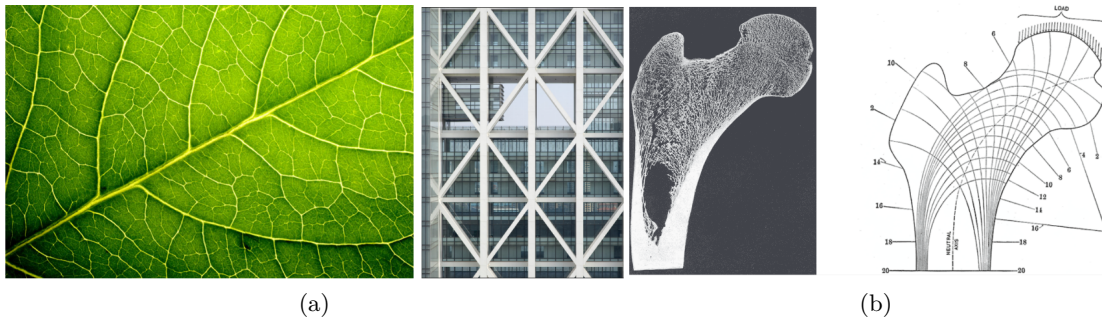
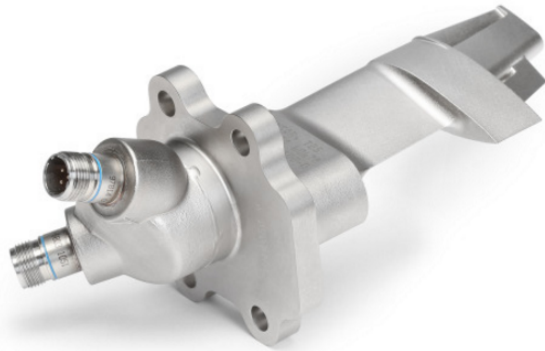


FIGURE 1.1: *a.) Ordered cellular reinforcement of a leaf. b.) Spongy bone aligned along the load paths seen in the femur.*

1.2 Metal Additive Manufacturing

Metal additive manufacturing (MAM) is a rapidly growing technology used largely for prototyping and more recently for low volume production where part designs are complex and high strength metals are needed. Through the use of MAM, engineers are able to utilize the design freedoms that come with 3D printing and at the same time, incorporate high strength materials into their parts. As the industry moves more towards 3D printing metal for production, a greater understanding of the performance of the materials and the process is needed. Right now, metal printers are not fast enough to compete in high volume manufacturing but for low to moderate volume parts that are difficult or costly to manufacture using traditional methods, 3D printing is a cost effective solution. Take for example gas turbine fuel injectors. These parts are usually made from multiple castings, which are machined and then welded together. General Electric are now using metal printing to manufacture the fuel injectors in their new LEAP gas-turbine engines [1].

There are many different process that accomplish the same goal of 3D printing metal the most commonly used are, Selective Laser Melting(SLM), Direct Metal Deposition(DMD) and Electron



(a)



(b)

FIGURE 1.2: *a.)GE's T25 compressor inlet temperature sensor printed from cobalt-chrome. b.)GE's gas turbine fuel injector also printed from cobalt-chrome.*

Beam Melting (EBM). Each process has its advantages and disadvantages, but because Cal Poly recently acquired an SLM 125HL machine, the focus of this review will be the SLM process. SLM works by directing a high powered (400W in the case of the SLM 125HL) fiber laser at bed of metal powder, the powder is then fully melted and joined with the layer below it and a new layer of powder is brushed over the print bed. This process of melting powder and recoating new powder is repeated over and over until a part is made, the process can be seen in Figure 1.3.

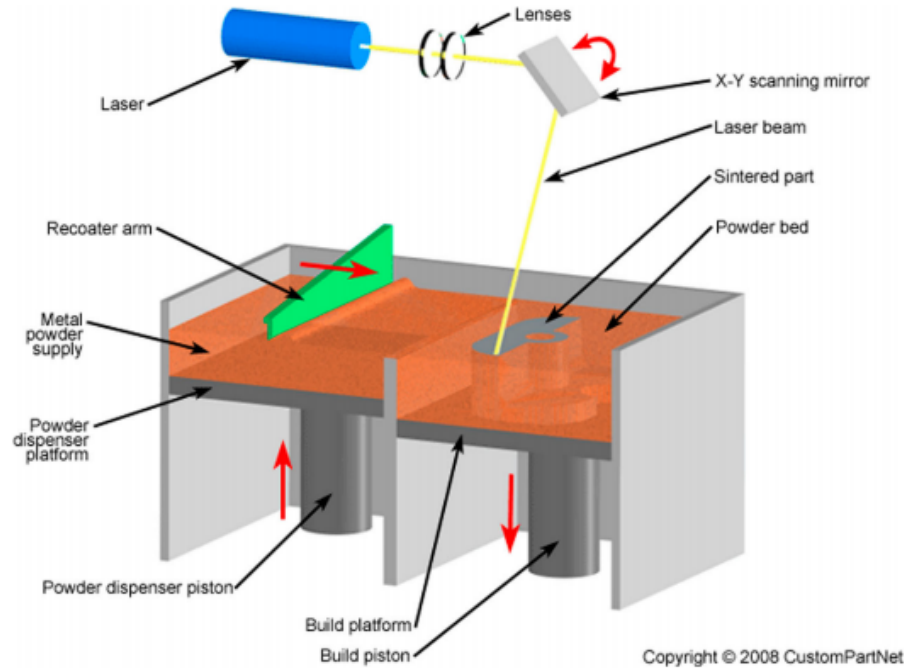


FIGURE 1.3: *SLM process schematic.*

Arguably all of the metal additive manufacturing technologies are in their infancy stages, but the SLM process which started in 1995 at the Fraunhofer Institute has progressed to become one of the most commonly used MAM technologies today. What makes SLM attractive is its ability to print aluminum and a wide variety of other metals with high precision and maintain feature sizes down to $140\ \mu\text{m}$ depending on the settings of the printer. However, the process is not without flaws, SLM is slow compared to casting and other traditional metal manufacturing methods, small amounts of porosity can be introduced, and the sizes of parts is limited by the build volume. These issues are constantly improving as the technology develops. For example, between 2005 and 2013 the speed at which you could print the same part became 50 times faster.

Chapter 2

Literature Review

This section explains the advances made over the last decade in microlattices and with SLM printed stainless steel to understand what has already been done and what still needs to be done.

2.1 Metallic Microlattices

The idea of metallic microlattices evolved from the work of Deshpande, Fleck, and Ashby on the mechanics of metal foams. Their paper, “Effective Properties of the Octet Truss Lattice Material” [2] on octet lattice properties was the first to extensively study the mechanics and properties of one specific metallic microlattice; the octet truss. Deshpande compares the properties of cast aluminum octet lattice samples analytically and experimentally with aluminum foams and concludes the specific stiffness and strength of the lattice material are much better than that of the foam. As previously mentioned the lattices have higher structural efficiency is due to a sort of mechanical advantage that the octet lattice structure has over the foam. The octet lattice has a stretch-dominated behavior while the foams have bending-dominated behavior as shown in Figure 2.1. This means that by using a truss-like lattice architecture, the members in the lattice are being loaded in tension and compression rather than bending. Metals are always stronger in tension than they are in bending. Deshpande did not release experimental data on the lattices but the paper revealed one of the primary advantages of lattice materials. After Deshpande’s work, SLM technology evolved leaps and bounds and metal lattices gained much more attention because of the ease at which they could now be manufactured.

In 2007, Santorinaios et al [3] studied the uniaxial compressive properties of 3D printed lattices with cell sizes of 1.25mm, 2.5mm and 5mm. The lattice he used was a simple cross braced vertical strut geometry shown also known as pillar textile shown in Figure 2.3, and the material used was SS316L. His conclusions were that the lattices with the smallest cell size, 1.25mm, had the highest compressive and shear strengths. This is expected because a smaller unit cell size means there are a greater number of members to carry the load, but also results in a higher density. So, the relationship between compressive strength has to do with density of the lattice. He also noted

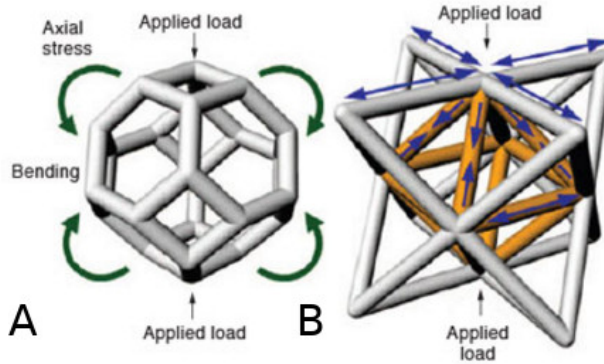


FIGURE 2.1: A) a unit cell of a bending dominate lattice under load B) versus that of the octet truss, a stretch dominated lattice, under loading.

the presence of manufacturing defects in the lattices. The struts which were around $100\ \mu\text{m}$ in diameter were not the desired cross-sectional cylindrical shape. There was also a high likelihood of local disconnections of struts at the nodes, underlining the need for more focus on controlling the morphology (i.e. the lattice's strut shape and surface characteristics). In 2010, Tsopanos [4] addressed the concern of the morphology and reported on the influence of processing parameters on the mechanical properties of SLM processed SS316L microlattices. For the first part of his two part study he printed single struts of diameters ranging from $150\ \mu\text{m}$ to $250\ \mu\text{m}$ at various laser powers and build angles to characterize the properties of the struts on their own. This would help inform computational models on quantifying the performance of lattices. The struts were found to have a modulus of $140\ \text{GPa}$ and a yield strength around $260\ \text{MPa}$. The strut build angle, which is the angle of the strut in relation to the build plate, had a small effect on the strength of the strut, as expected the lower build angles had lower strength values and the difference between 45° and 90° was around $30\ \text{MPa}$. It was noted that larger variations in diameter occurred at lower build angles as well. The second part of his study was testing the compressive properties of BCC (Body Centered Cubic) microlattices built with three laser exposure times (500ms, 750ms and 1000ms) and corresponding laser power settings. His findings, were that laser power had the most significant effect on the strength of the strut and an exposure time of 750ms resulted in the best properties. The drop in strength with lower laser powers is likely due to partial melting of powder particles causing early failure.

Relative density increases with laser exposure and power, also indicating more complete melting. Yield strength and modulus of the lattices increases linearly with relative density. In 2013, Gumruk reported a similar finding on three variations of printed steel BCC lattices. In his paper [5] he reported that again, the smaller the lattice cell had the stronger compressive strength and that in compression lattice geometries with a vertical strut were far stronger. Figure 2.2, are idealized stress strain curves that show, first, an elastic region, followed by a region of strain hardening up to a densification strain when the lattice struts are fully compressed against each other. The difference in performance between the bending dominated and stretch dominated lattice, are that in the elastic region, stretch dominated will show high stiffness and high yield strengths. He also reported that defects, such as voids and discontinuities in the lattice, due to the printing process, contributed

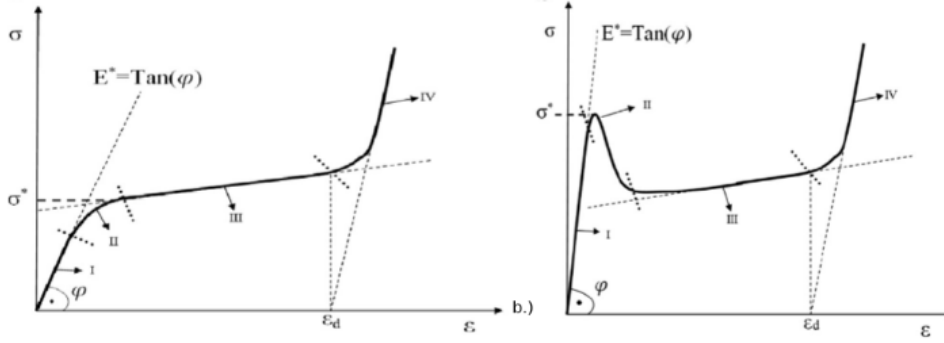


FIGURE 2.2: *Typical stress strain curves of bending dominated lattices and b.) stretch dominated lattices. [5]*

to subpar compressive strengths in all the lattice samples he tested compared to foams. In 2013, Contuzzi et al [6] attempted to estimate the lattice properties by using nonlinear finite element (FE) analysis to find the Von Mises strength of 6 different lattice unit cells. He determined that the pillar textile geometry is the best in compression and the second lightest geometry according to his FE models shown in Figure 5. He uses 18 Ni Maraging 300 steel to test the compressive strength of the pillar textile lattice with and without solid columnar reinforcements. He concluded that the compressive strengths of the lattices increased almost linearly with density. However, Contuzzi reports that the larger cell size (3mm) had a higher specific strength than did the smaller (2mm). With the increase in cell size, the strut thickness increases and the strut length increases, and because the struts exhibit buckling failure under compression, the benefit of an increase in thickness of the strut outweighs the drawback of an increase in length of the strut. Meaning in the case that the lattice undergoes buckling failure, smaller cell sizes are not always better.

Some interesting nuances about these lattices are that the failure modes that are seen in BCCZ lattices are size dependent [5]. Larger cell sizes show typical stretch dominated collapse where a peak stress value is seen before the strain hardening plateau, however with smaller cell sizes $< 1.5\text{mm}$ the lattices exhibit bending dominated collapse behavior. This is likely due to the fact that the smaller lattice struts are too short to buckle. Another observation worth noting is that as cell size decreases, relative density increases and strength values increase. And with smaller cell sizes densification strains go down. Most BCC lattices and other variations of those lattices experience diagonal failure characteristic of samples that experience plane stress/strain. The samples in this study were constrained which means the lattice samples that have solid top and bottom sections. The difference in failure behavior between constrained and unconstrained samples in BCC lattices is almost negligible in terms of peak stress and stiffness. The only difference is that failure is initiated in the center of the lattice in the constrained samples.

Because there are no direct comparisons between lattices experimentally, it is hard to tell which lattice geometry performs the best. Although multiple studies reported on compressive strength values they are not comparable because of differences in tests, sample geometries, and print quality. However according to Contuzzi's theoretical models the pillar textile geometry is the best of the six he modeled however he did not include the BCCZ lattice geometry or the isotruss [7] lattice

which are both highly studied lattices. So, there is a need for a side by side comparison of the four lattices, BCCZ, pillar textile, isotruss and octet truss. Additionally, for each of those four lattices there should be two cell sizes 2.5mm and either 1.25mm or smaller since the properties and failure modes of the lattices are very different depending on the size of the cell. Finally, since there is not a huge difference between constrained and unconstrained lattices, the samples should be printed as constrained.







	$\rho = \frac{V_{\text{cell}}}{V_c} = 0.263$ $\beta = \frac{S_{\text{cell}}}{V_{\text{cell}}} = 8.335 \text{ mm}^2/\text{mm}^3$ $V_{\text{cell}} = 7.1 \text{ mm}^3$ $\sigma_{\text{VM}} = 1115 \text{ N/mm}^2$ $R = 1509 \text{ N}$		$\rho = \frac{V_{\text{cell}}}{V_c} = 0.286$ $\beta = \frac{S_{\text{cell}}}{V_{\text{cell}}} = 6.011 \text{ mm}^2/\text{mm}^3$ $V_{\text{cell}} = 7.7 \text{ mm}^3$ $\sigma_{\text{VM}} = 1096 \text{ N/mm}^2$ $R = 461 \text{ N}$
Pillar textile		Diamond lattice	
	$\rho = \frac{V_{\text{cell}}}{V_c} = 0.263$ $\beta = \frac{S_{\text{cell}}}{V_{\text{cell}}} = 6.345 \text{ mm}^2/\text{mm}^3$ $V_{\text{cell}} = 7.1 \text{ mm}^3$ $\sigma_{\text{VM}} = 1115 \text{ N/mm}^2$ $R = 1158 \text{ N}$		$\rho = \frac{V_{\text{cell}}}{V_c} = 0.263$ $\beta = \frac{S_{\text{cell}}}{V_{\text{cell}}} = 4.323 \text{ mm}^2/\text{mm}^3$ $V_{\text{cell}} = 7.7 \text{ mm}^3$ $\sigma_{\text{VM}} = 1101 \text{ N/mm}^2$ $R = 991 \text{ N}$
Diamond textile		Kagome	
	$\rho = \frac{V_{\text{cell}}}{V_c} = 0.319$ $\beta = \frac{S_{\text{cell}}}{V_{\text{cell}}} = 6.131 \text{ mm}^2/\text{mm}^3$ $V_{\text{cell}} = 8.6 \text{ mm}^3$ $\sigma_{\text{VM}} = 1109 \text{ N/mm}^2$ $R = 1493 \text{ N}$		$\rho = \frac{V_{\text{cell}}}{V_c} = 0.138$ $\beta = \frac{S_{\text{cell}}}{V_{\text{cell}}} = 11.165 \text{ mm}^2/\text{mm}^3$ $V_{\text{cell}} = 3.7 \text{ mm}^3$ $\sigma_{\text{VM}} = 1112 \text{ N/mm}^2$ $R = 538 \text{ N}$
Pillar octaedral		Square collinear	

FIGURE 2.3: Comparison of some lattice geometries. Properties in order are relative density, area density factor, volume of the cell, Von Mises stress from FE model, compression load before initial failure. [6]

2.1.1 Summary

- Stretch dominated lattices are stiffer and have higher yield strength than bending dominated lattice geometries.
- For compression, number of vertical struts is the most important factor contributing to strength.
- Relative density increases linearly with laser power and exposure time.
- Yield strength and modulus increases linearly with relative density.
- Main variables of lattice geometry to consider in making these lattices: strut diameter, strut shape, radius of node connections.
- Still not known which parameters/geometries are best for specific strength.

2.2 Metallography and Morphology

The main focus of this work is to characterize the stainless steel material printed by the SLM here at Cal Poly. In addition to mechanical testing, the metallurgy and morphology of 316L will be studied. Printed metals tend to have better mechanical properties compared to castings of the same material. For example, as-printed selectively laser melted AlSi10Mg has a 40% higher yield strength and 58% increase in elongation than as-cast AlSi10Mg. Differences between their microstructures cause this increase in yield strength and elongation, so understanding those differences and how they occur is extremely valuable.

It is well-known that the solidification rate of liquid metal controls its final microstructure. The metallurgical results of selective laser melting is similar to what is seen in traditional welding processes; very rapid solidification rates on the order of $130^{\circ}\text{C}/\text{sec}$ [8]. Often times the SLM process is described as building a part with welds, layer by layer. The fast cooling rates are due to the high energy density of the printer's 400W laser; this means that there is a lot of energy that is concentrated in a small area, generally ($140\mu\text{m}$). Second, the laser can scan at speeds much faster than possible with other fusion joining methods, so the laser only interacts with the powder for short time. This heat is conducted away from the molten steel via the powder bed, and convected away by the gaseous argon in the build chamber. Fast cooling does not give the grains time to grow and as a result grains are much smaller than cast stainless steel. According to the Hall-Petch equation, smaller grains block dislocation movement and increase the strength of the material. This is the main advantage of the SLM process from a metallurgical standpoint.

In a study done by Zhongji [9], X-Ray Diffraction (XRD) analysis was performed to determine the phase composition of the printed steel. The XRD analysis showed that printed 316L has a high amount of FCC phase, and some BCC phase. The FCC phase is austenite and the BCC phase is retained δ -ferrite. It was not found to contain any martensite. Additionally, because of the broad peaks in the XRD readings it is thought that there are residual stresses in the part that slightly alter the bond length readings. The δ -ferrite is retained because it is not given enough time to transform into austenite. Zhongji carried out Transmission Electron Microscopy (TEM) to observe the microstructure of the SS316L. The steel has a cellular subgrain microstructure shown in Figure 2.4, and epitaxial growth is evident along scan path. Epitaxial growth is grain growth upon solidification and is commonly seen in laser welds. The average grain size observed was $1\mu\text{m}$, and the hardness of the microstructure was roughly 217HV.

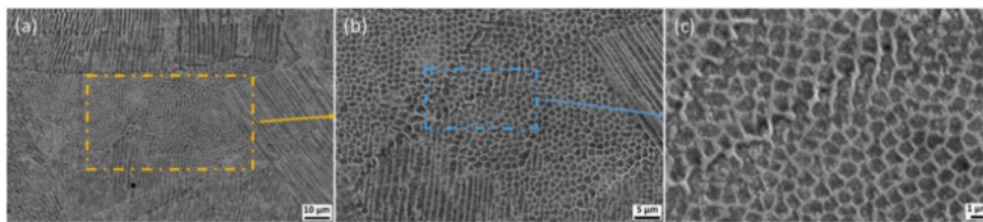


FIGURE 2.4: TEM imaging shows cellular subgrains in all three photos. [9]

2.3 Qualifying and Characterizing 3D Printed Materials.

One major issue to bring up when studying the practical application of 3d printed metals is how to implement them responsibly in safety critical applications like commercial flight. The Federal Aviation Administration(FAA) has testing requirements for materials(14 CFR 25.603) used in airplanes depending on their level of criticality or importance with respect to the overall function of the airplane. For materials like metals and composites these tests and procedures are well defined. For example, there is a roadmap so to speak for what tests need to be performed to certify a new aluminum alloy for your airplane. But for materials like 3D printed metals, no such roadmap exists yet. Under the FAA's rule for fabrication methods (14 CFR 25.605), "each new fabrication method must be substantiated by a test program." So it is up to the Original Equipment Manufacturers to come up with these test programs. Coming up with standard test procedures for these materials would enable more efficient, and safer qualification and certification for additive materials. [10]

At high levels of part criticality, fatigue and fracture mechanics become the most important metrics for safety. For relatively homogenous materials, understanding these mechanisms are still highly complex but the methodology exists such that crack initiation and growth can be monitored and managed. Currently, there is a lack in understanding of the relationship between processing parameters, material microstructure, defects size, defect population and fatigue and fracture behavior of both leading metal additively manufacturing process types (powder bed fusion and direct energy deposition).

Current test methods may not be applicable to additively manufactured materials because they generally assume material homogeneity. One way to get around this is to use a probabilistic approach to damage tolerance where statistics are used to predict the likelihood of fracture based on the population and distribution of the inherent defects (i.e. porosity or unmelted powder). Currently the AM industry has identified four challenges that need to be overcome to characterize the fatigue and fracture behavior of 3d printed metal, they are:

- Presence of defects
- Anisotropy
- Surface roughness
- Similarity of test coupons

Much more characterization is needed for additively manufactured materials to get flight time and start making aircraft more efficient.

Chapter 3

Experimental Procedure

The plan for characterizing the material was to gather as much information on the material as possible to best inform students at Cal Poly about the printed material so future works would have 'baseline' data. Additionally, a side by side comparison of four microlattices was carried out because comparing specific stiffness on an imperial basis had not been done with these geometries.

Characterization of a material is a very vague statement, but to most it means understanding one or more of a material's chemical or physical characteristics to better understand how to improve the materials response to mechanical or environmental conditions. Characterization was accomplished by examining three aspects of the material, its microstructure, mechanical properties, and physical aspects such as porosity, warp, and fracture behavior. A number of characterization techniques were used:

- SEM/EDS Analysis
- Archimedes Density
- Vickers Hardness
- ASTM E8 Mechanical Testing
- XRD analysis

3.1 Fabrication of Printed 316L Samples

3.1.1 SLM Prints

Oversized tensile specimens and density cubes were printed using SLM's 125HL printer and SLM's 316L stainless steel powder. Three builds were carried out, each fit four oversized bars oriented in the XY direction as shown in Figure 3.1. The printer's settings, commonly referred to as printer parameters, control the resultant microstructure and mechanical properties of the parts. The same printing parameters were used to build every tensile bar and density cube used in this study. These parameters are shown in Table 3.1. The bars were rotated 2° from the Y axis to minimize

the likelihood of errors during the recoating process. Ideally, parts would be removed by EDM machining however this process was not available. Parts were raised 5mm above the build plate with square support structure and removed using a horizontal bandsaw. Aside from heat treatment, no other post processes were done to the builds.

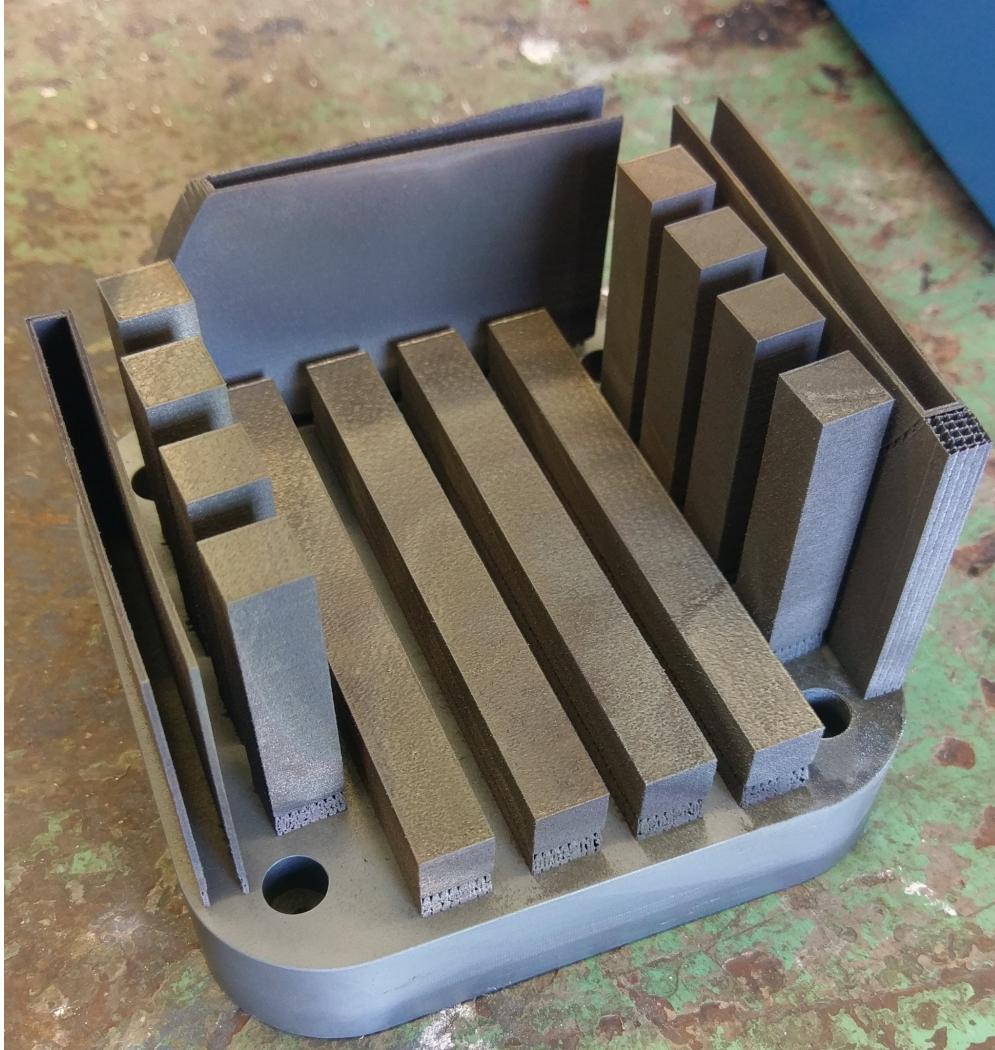


FIGURE 3.1: *SLM build plate with tensile bars attached in the XY direction after heat treatment. Note: this build failed before the Z direction tensile bars could be finished.*

TABLE 3.1: *Settings for the core hatching parameter. The core hatching parameter is how the main volume of metal powder is melted, and makes up the entirety of the tensile bar. Power density was calculated using Equation 1.*

Laser Power W	Scan Speed mm/sec	Layer Size Microns	Hatch Distance mm	Power Density J/mm ³	Build Plate Temp °C
950	230	30	.06	2111.1	120

$$PowerDensity = \frac{LaserPower}{ScanSpeed \times Layersize \times HatchDistance} \quad (1)$$

3.1.2 Heat Treatment

The heat treatment that was chosen was a full anneal carried out at 1040°C for 4 hours. A full anneal was chosen to remove all residual stresses and minimize anisotropy caused by the differences in solidification. Parts were kept on the build plate so as not to introduce warp which could prevent tensile bars from being machined. Ideally a vacuum furnace would be used so that no oxidation would occur however no such oven was available. A Rapid Temp Furnace was used instead. To prevent the introduction of oxides and other intermetallics from forming, the build plate was sealed in a stainless steel bag to oxidize sacrificially. The sealed build plate was taken out of the furnace then air cooled to room temperature before being removed from the bag.

3.1.3 Machining

Initial machining was attempted on the density cubes using standard tooling and spindle speeds. This was unsuccessful as the material was too tough and high speed steel endmills would break even at low feed rates. Machining was done on a Haas Mini Mill using a high rake angle 5 flute carbide endmill, and the recommended speeds and feeds were calculated based on the hardness of the material. Spindle speed was set at 3818 rpm and the feed rate at 22.9 fpm for a .25" diameter endmill. The final dimensions of the ASTM E8 Subsize specimen are shown in Figure 3.2.

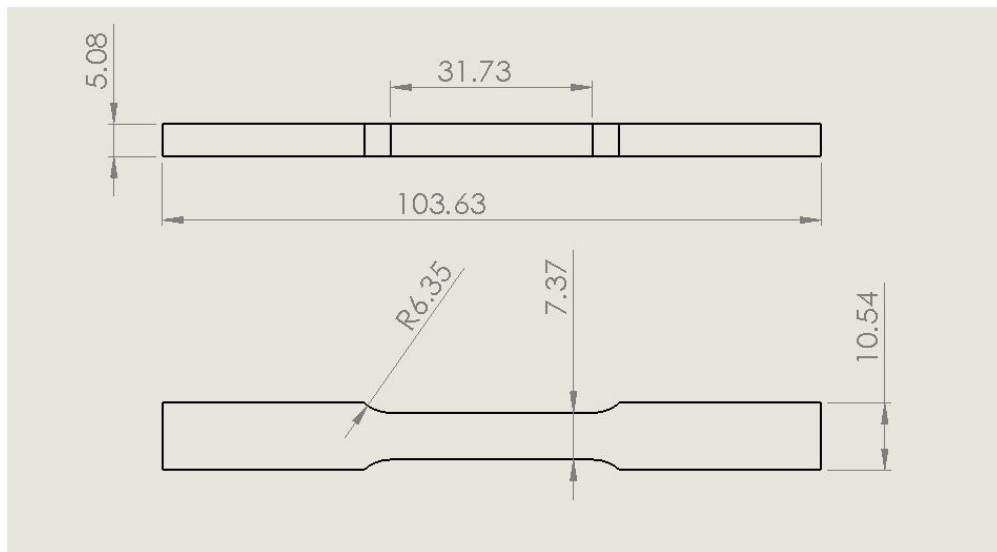


FIGURE 3.2: An Engineering drawing of the tensile bars after being machined.

3.1.4 Lattice Selection

The lattices tested in this study are shown in Figure 3.3. The goal with the microlattices was to determine which would make the best core material, so lattices were selected based on their specific stiffnesses. Octet Truss was selected because it is the most widely studied and one of the first microlattices to be theorized[Deshpande]. BCCZ was selected because it was the best performing lattice in Gumruk’s study. Pillar Textile again was the best performing in Contuzzi’s study and Isotruss was selected because it is a geometry currently being studied at LLNL and is the most isotropic behaving lattice to date. FEA was attempted on the unit cells of each geometry to understand the unit cell’s theoretical stiffness. However, two issues prevent the FEA data from being useful. The first is how the unit cells are meshed, to be a good comparison, the meshing should be similar, however the software used to mesh the unit cell models did each differently and some resulted in singularities or odd uneven meshes. The second issue is with analyzing only one cell, most lattices get their strength from interactions with other cells. So, to be effective many cells would have to be modeled together, which would require much more computing power.

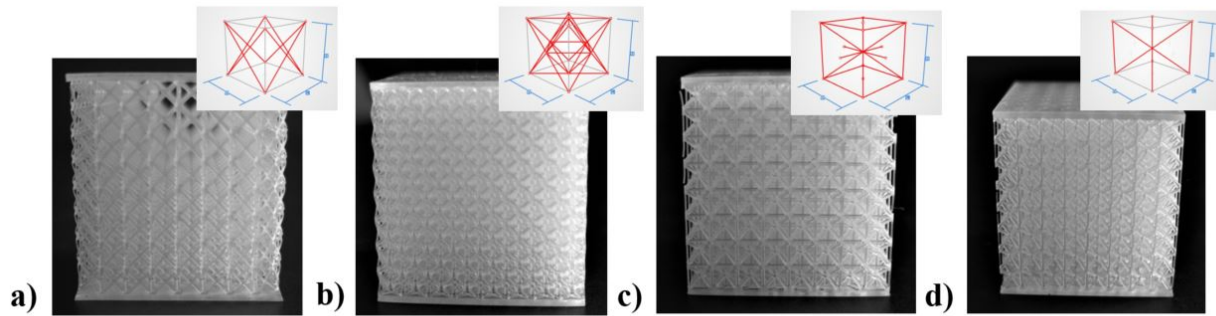


FIGURE 3.3: A) Pillar Textile B) Octet Truss C) Isotruss D)BCCZ.

3.1.5 Lattice Generation, Printing and Testing

Lattices first had to be modeled and special software was needed. Solidworks and other parametric modeling softwares are not able to process the complex geometries using standard computer processors. Autodesk Within and Element 3D are two design softwares that are able to adequately model the microlattices. Autodesk Within has every feature needed to fully customise just about any cellular design. Within features built-in FEA and optimisation software, however it was not available for students to download. Element 3D by nTopology, has all of the features for generating cellular designs that Autodesk Within has, but with a more friendly user interface. Element 3D is free for students, however it does not have the FEA and optimisation features which are useful when designing lightweight functional components. Figure 3.4 shows the process of generating custom lattices using the Element 3D. The lattice samples were printed with a 0.5 mm solid plate to constrain the top and bottom of the lattice. The sample’s total dimensions were 20 mm x 20 mm x 21 mm.



FIGURE 3.4: A flowchart of the lattice design process.

Once each lattice was designed an .stl was generated. Even with a lattice as small as these samples, the file sizes for the stl's were generally above 500MB making them hard to manipulate using printer software. The lattices were printed using an Autodesk Ember, this printer uses Digital Liquid Projection (DLP) to cure a photopolymer in a liquid bath. The parts are pulled out of the bath upside down. The build plate on the Ember is quite small at 64 mm by 40 mm by 134 mm, however two samples could easily be printed at the same time. The polymer used is called HexaneDiol DiAcrylate (HDDA).

The samples were compression tested on a Shimadzu test frame with a 5kN load cell. The crosshead displacement speed was 3 mm/min. Tests were run until densification strain was reached. Force vs Extension was measured for each lattice. Stress, strain and modulus were obtained from the force/extension data and specific stiffness was calculated using Equation 2.

$$\text{Specific Stiffness } (m^2s^{-2} \times 10^3) = \frac{\text{Young's Modulus } (Pa)}{\text{Density } (g/cc)} \quad (2)$$

3.2 Testing

3.2.1 Tension testing

ASTM E8 tensile testing was carried out using a 150kN Instron Test frame. The machined, subsize E8 tensile bars were pulled at a crosshead displacement speed of 3 mm/min. Specimen dimensions were input to calculate stress and strain from load and extension data. Elongation data was collected using an Epsilon contact extensometer.

3.2.2 Hardness

The hardness of both the heat treated and as-printed material was tested using a Buehler Wilson 2000 hardness testing machine on the Rockwell B scale and then converted to Vickers hardness scale. Hardness is useful in that it is measured locally and provides comparative data about the printed materials anisotropy due to thermal effects. 6 measurements were taken on each side of the

density cube as shown in Figure ??fig:harddiagram).

3.2.3 Porosity

For PM (Powder Metallurgy) parts, densification is usually measured according to ASTM B311 where the mass of a cube is measured in air and water. In this study, porosity was measured using a method similar to the Archimedes method. These density cubes were machined down to eliminate any inaccuracies caused by the uneven printed surface. The new dimensions of the cube were measured and the volume was calculated. The cubes were then weighed on a scale to find the mass, then the apparent density was calculated from a theoretical density of 7.985 g/cc to determine % porosity.

3.3 Metallography

Understanding the microstructure of the material is of significant importance to this study. Mechanical performance is derived partly from the grain size and orientation. So, identifying and controlling the grain structure by changing the printer's parameters is extremely valuable. To get an understanding of the grain structure, density cubes (both as-printed and heat treated) were sectioned using an abrasive chop saw. Three cuts were made so as to expose the XY, XZ and YZ planes. The cut surfaces were then mounted in Bakelite, and sanded down to 600 grit before being polished using 3 μm polycrystalline abrasive. After a clean polished surface was achieved, the thin layer of worked metal was removed by an electrolytic etch using oxalic acid. The electrolytic setup used was an old Beuhler power supply that provided 4V for 1:45 minutes to the 316L samples.

3.3.1 SEM

The Cal Poly MATE department's FEI Quanta 200 Scanning Electron Microscope (SEM) was used to image the outside surface of the material, the microstructures of both the heat treated and non heat treated samples, and fracture surfaces. Settings of the machine varied depending on the image being taken and are displayed at the bottom of each image.

Chapter 4

Results and Discussion

This section presents all of the data collected on Cal Poly's SLM printed 316L stainless steel and the lattice cubes and discussion of these results.

4.1 316L Stainless Steel Characterization

4.1.1 Printer Functionality

The SLM 125HL was non-operational for the majority of this project, which limited the number of samples able to be tested. Aside from the initial setup of the printer, there were instances where parts on the machine would break caused period of down time. The system that caused the most trouble was the powder dispensing system. After the first successful build, four tensile bars and two density cubes were removed from the build plate without heat treatment. The high energy required to melted steel causes steep thermal gradients, which upon cooling, result in residual stresses. Because the bars had such high residual stresses, and were thinner in the middle they warped significantly. So much so, that they were unable to be fixtured in the CNC mill. This highlighted the importance of performing a heat treatment after the build was finished while parts were still attached to the build plate. Ideally, the parameters of the printer would be adjusted to minimize this warp but parameter optimization is outside the scope of this project. The heat treatment would eliminate the residual stresses that cause warp in the part, but also negate the advantages of refined grain structure. Regardless after heat treatment there was considerably less warping in the bars. Printing aluminum and titanium is far more reliable than printing with stainless. However because both of these powders are reactive they can combust at room temperature when ignited by a spark. So, it makes sense that at Cal Poly we are not allowed to print reactive metals.

4.1.2 Surface Morphology and Porosity

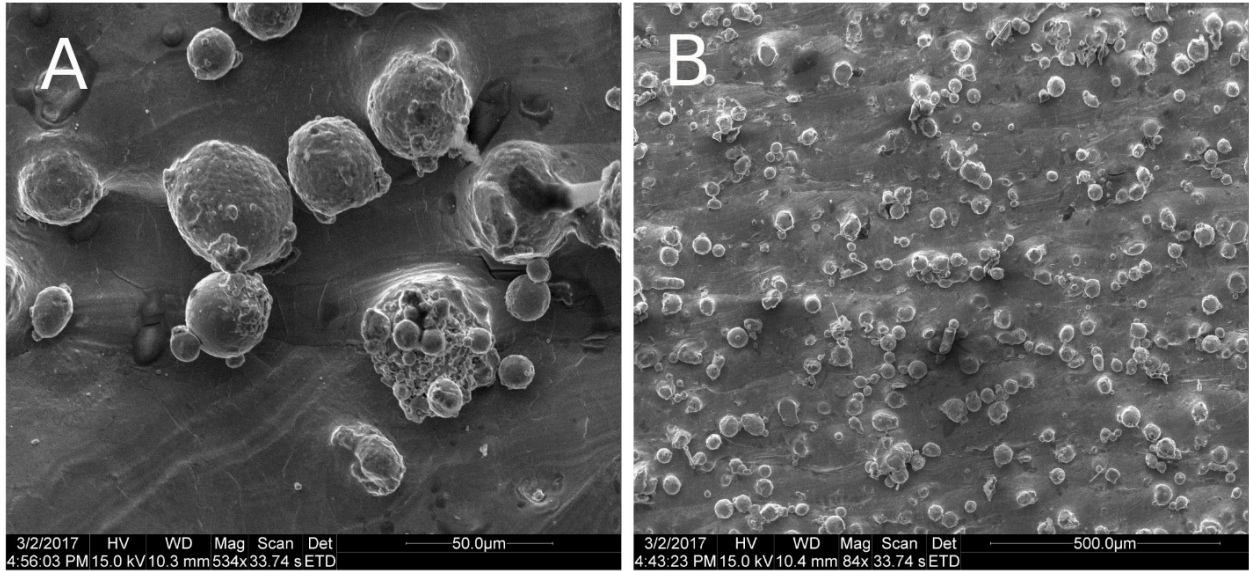


FIGURE 4.1: A) Partially melted powder particles can be seen attached the surface of the part. Attached to the printed surface are partially melted, powder particles. B) From a distance these powder particle trap light and give the stainless steel parts their matte finish.

TABLE 4.1: Porosity calculated based off of density measurements obtained via the Archimedes method. The porosity of the third build is abnormally high. However upon inspection of the fracture surface of this build, there was a large population of voids, so it is possible this number is reasonable.

Density cube	Weight (g)	Volume (cm ³)	Density (g/cc)	Porosity (%)
Build 1	24.764	3.123	7.929	0.89
Build 2	14.394	1.818	7.913	0.90
Build 3	13.951	1.819	7.665	4.11

Porosity was evident in the material at different levels. Under 1% porosity is quite common for SLM, and in the earlier builds porosity was 0.89% and 0.90%. A higher amount of porosity, 4.11%, was observed in the later build (build 3) see Table 4.1. It is possible that the density cube captured a higher population of voids than was representative of the print quality. In the fracture surfaces of the bars printed on build 3 seen in Figure 4.8a, voids are present in high concentration and in a regular pattern. This proves that the voids were caused by an error in the recoating step. This issue should be addressed by changing the parameters of the machine. Upon examining nonmachined parts, porosity was observed in the contour path (outside edges of the part). The printer's laser and speed setting change when melting the contour path, due to that change more voids were introduced. As a technology SLM has a long way to go to achieve production level repeatability for highly critical parts. Still, SLM printers that have been properly tuned are extremely reliable.

4.1.3 Microstructure

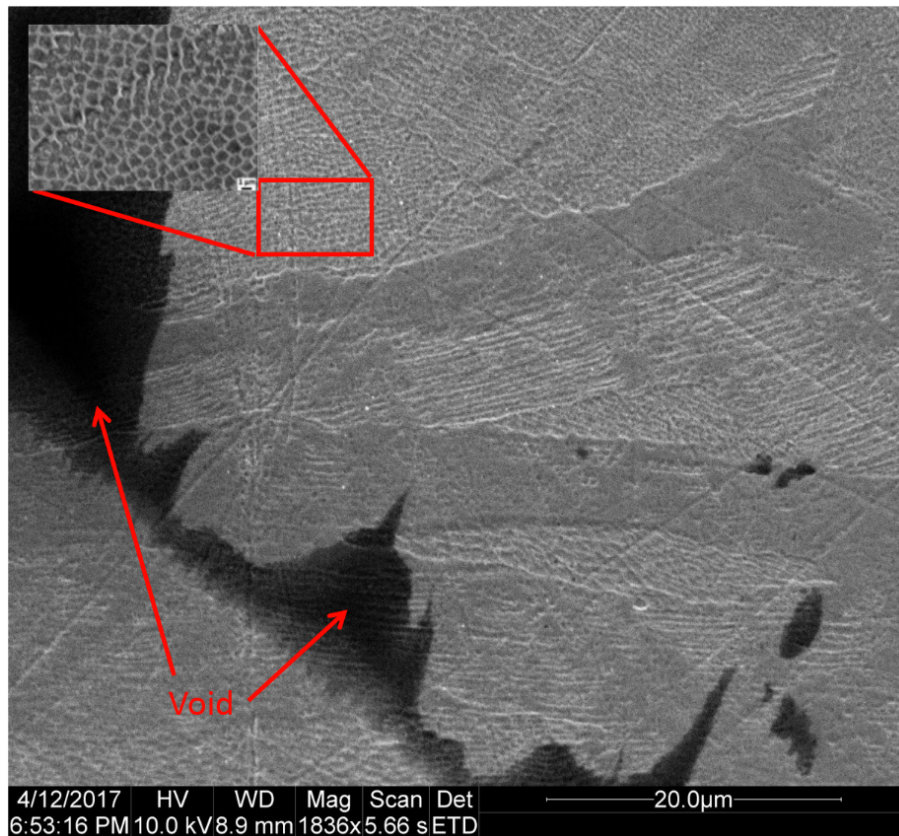


FIGURE 4.2: *Shown here is a void likely caused by imparital melting of powder particles. Around the void the acicular δ -ferrite subgrains are clearly visible. The δ -ferrite are the circular ridges.*

The microstructure of the as-printed and heat treated 316L were examined and are shown in Figure 4.2. The as-printed microstructure showed cellular subgrains which are formed because of the precscence of a δ -ferrite phase. 316L is an austenitic stainless steel meaning that under normal processing conditions there should be only one phase, austenite. However a small amount of delta ferrite is retained because of the non-equilibrium cooling that the material sees during the SLM process. Welding is another process where similar non-equilibirum cooling occurs. A Schaffler diagram 4.3, used for determining the rough amount of phases in welded stainless steels shows that there woud be roughly 5% δ -ferrite for 316L. The δ -ferrite shows up as tubes surrounding the austenite phase which was observed in this study, see Figure 4.2, and in other works [11]. This structure is not seen everywhere in the metal, so there is variation of grain structure likely due to varying in cooling rates at different locations in the part during printing. Ferritic stainless steels have higher stiffness but are generally less ductile, while austenitic stainless steels have higher strength and ductility and are therefore tougher.

Looking at the mechanical performance of Cal Poly's heat teated 316L, there are signs of δ -ferrite being present. As shown in Figure 4.6 Cal Poly's 316L has much higher stiffness than other heat

treated material, lower ductility and lower yield strength characteristic of a material with higher amount of ferrite.

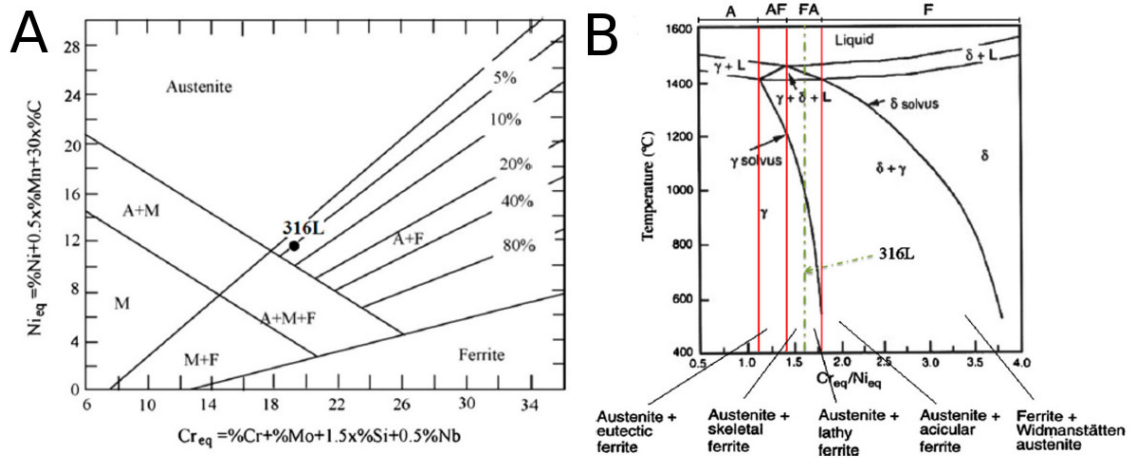


FIGURE 4.3: A) A Schaeffler diagram, shows the phase composition of welded 316L. B) A pseudo-binary phase diagram plots 316L based on its chromium/nickel equivalent. [12]

The heat treated microstructure was not able to be properly viewed optically. A different etch, Ralph's Solution, might have aided in the examination of the microstructure. The δ -Ferrite phase is magnetic and interestingly, both the as-printed and heat treated density cubes responded to a magnetic field. The full anneal on the heat treated part should have allowed all of the magnetic ferrite to transform to non-magnetic austenite. The heat treated samples were air cooled, however since chromium and molybdenum take so long to diffuse, there may still be trace amounts of δ -ferrite in the material.

4.1.4 Hardness

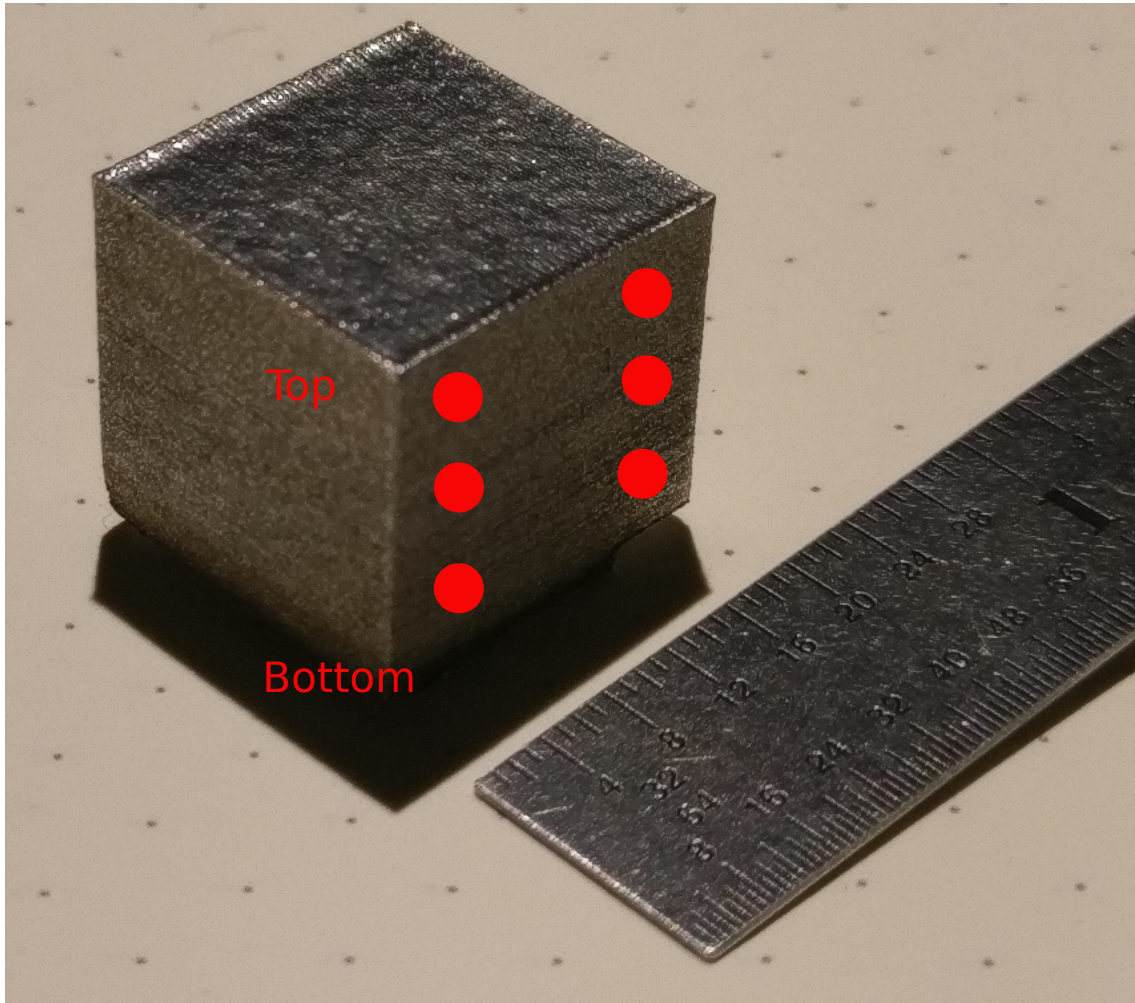
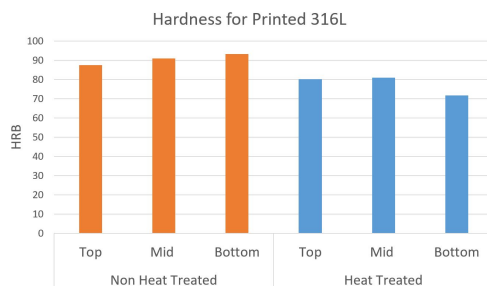


FIGURE 4.4: A density cube is marked with red dots where hardness measurements were taken in relation to the top and bottom of the cube.

TABLE 4.2: Hardness of as-printed surface of heat treated and non-heat treated 316L stainless steel. The values shown in this table are averages of the hardness of 6 density cubes, each tested in the same manner.



Average Hardness (HRB)		Standard Deviation
HT	87.55	6.21
Non-HT	90.96	3.32
Non-HT (Reported by SLM)	93.25	–

4.1.5 Mechanical Testing

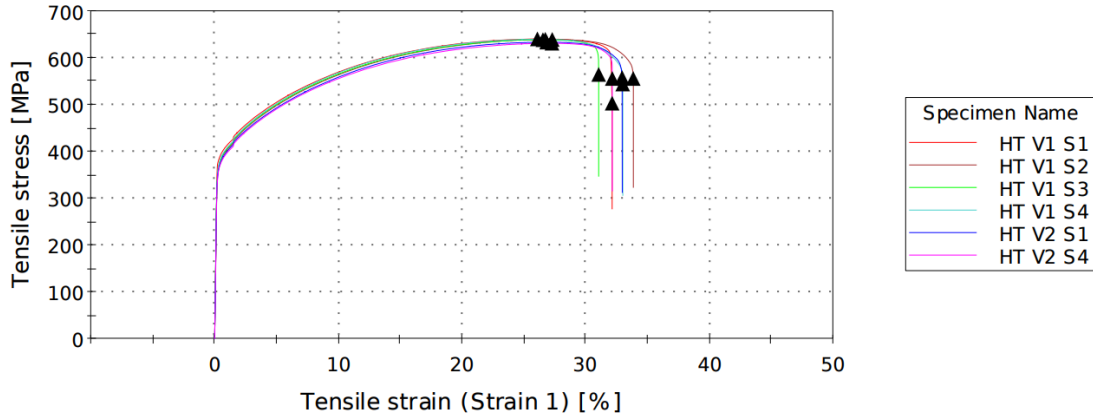


FIGURE 4.5: *The stress-strain diagram of the heat treated 316L material. Samples 6 and 7 were excluded because of an error in extensometer reading.*

TABLE 4.3: *Tensile test results from heat treated tensile bars.*

	avg.	std.
Young's Modulus (GPa)	207.2	6.85
Offset .2% Yeild Strength (MPa)	375.87	7.3
Ultimate Tensile (MPa)	636.87	3.39
Elongation (%)	32.45	0.96

TABLE 4.4: *Mechanical property comparison of Heat Treated material from this and others' studies to SLM's published properties and wrought 316L properties.*

Material Property	As-Printed (Data from SLM)	Heat Treated (Sistiaga)	Heat Treated (This Study)	Wrought 316L (Matweb)
Young's Modulus (GPa)	184	-	207.2	193
Yeild Strength 2% Offset (MPa)	519.0	360	375.87	290
Ultimate Tensile (MPa)	633	595.0	636.87	558
Elongation (%)	30	45	32.45	50

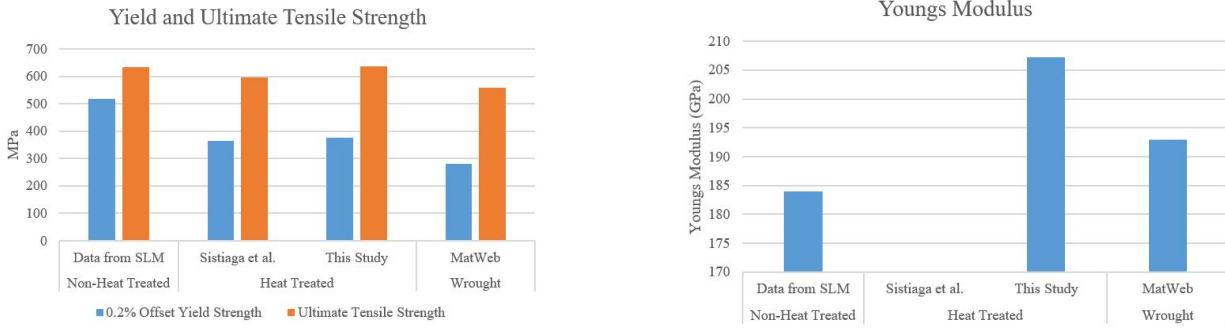


FIGURE 4.6: Graphical comparison of relevant mechanical properties.

4.1.6 XRD Analysis

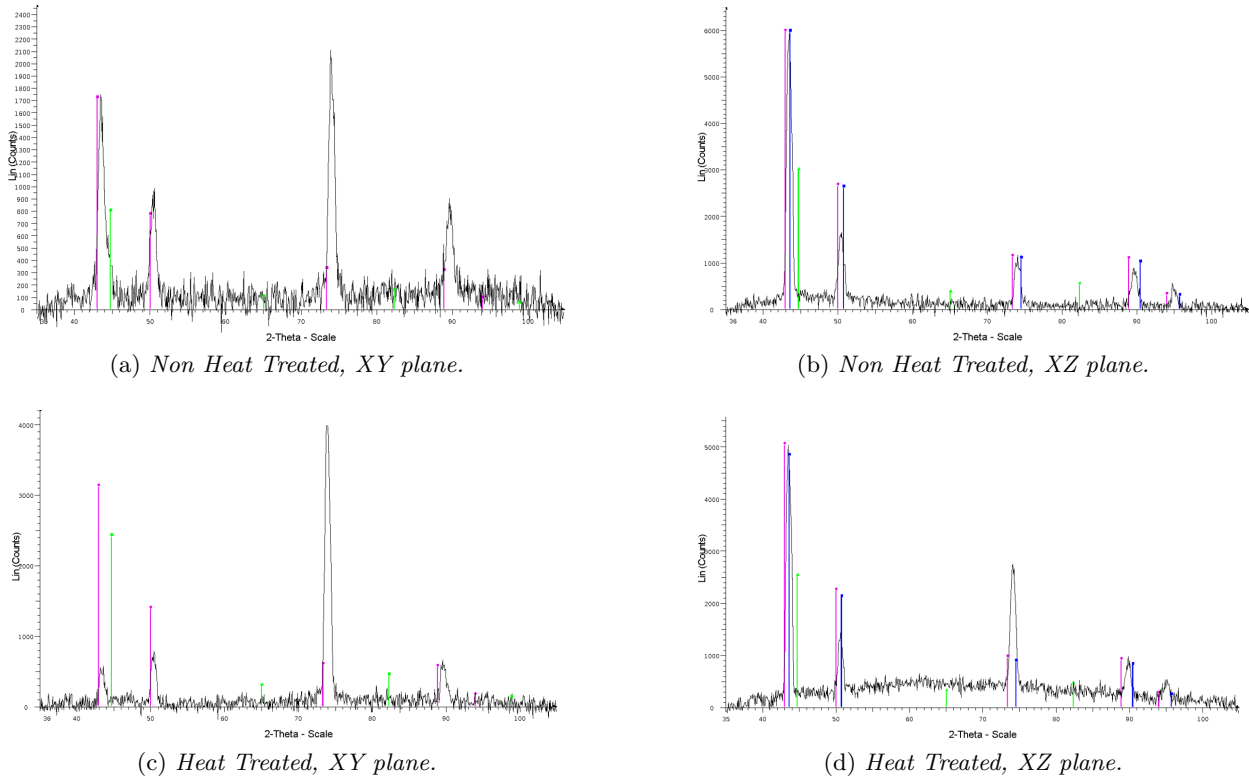


FIGURE 4.7: Purple lines on the XRD spectral results represent the lattice parameters of FCC iron (Austenite). Green lines represent BCC iron (δ -Ferrite). Notice the intensities of the peaks differ with heat treatment and direction. Peaks of all samples are shifted to the right. BCC phase do not appear present upon first inspection.

Differences in relative FCC (austenite) peak intensities between XY and XZ samples indicating grain orientation or 'texture'. This was interpreted as preferential orientation of grains in both the heat treated and as-printed samples. Preferential orientation makes sense because of the anisotropic nature of the SLM process. The peaks were also shifted in both the as printed and heat treated

samples indicating a different lattice parameter, which could be caused by residual stresses. Additional XRD analysis should be carried out, as it was unclear from the analysis that either samples had δ -ferrite phase present.

4.1.7 Fracture Images

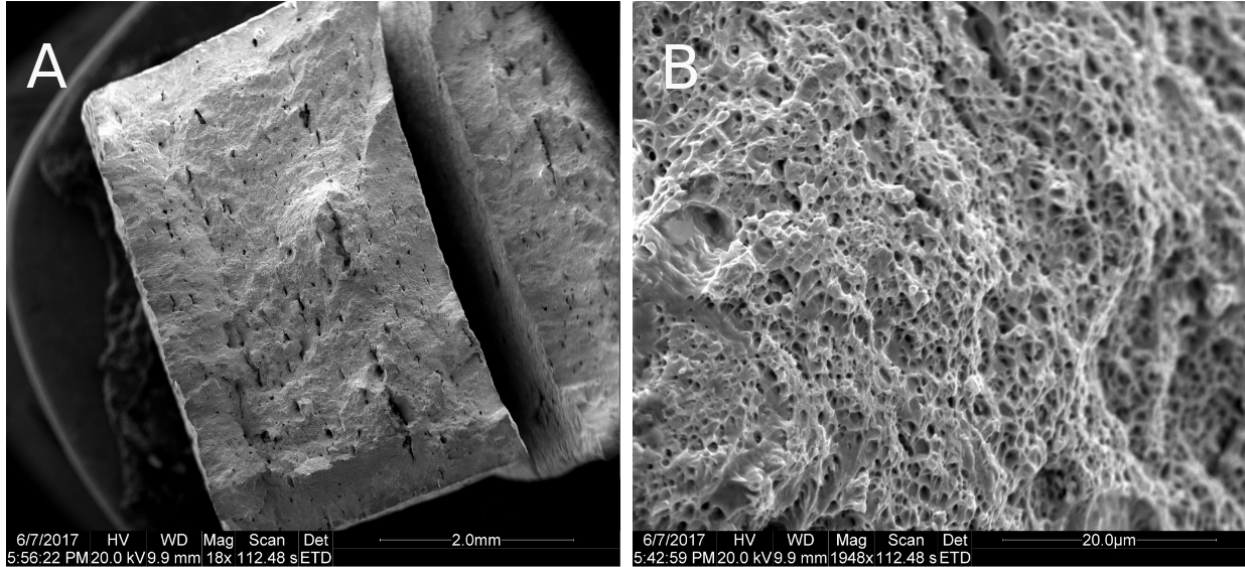


FIGURE 4.8: *A) Voids can be seen in the fracture surface. B) At higher magnification dimples can be seen, indicating ductile fracture.*

The fracture surface of the tensile bars showed clear signs of ductile fracture. The primary indicator was the "dimpled" surface. Shear lips were present on some of the samples indicating that the sample experienced plane stress and fracture was not prematurely initiated from a crack or pore. However some of the failures could be traced back to a large void on the surface of the part and did not have shear lips. Microvoids can be observed at the bottoms of the "dimples" shown in Figure 4.8.

4.1.8 Microlattice Compression Testing

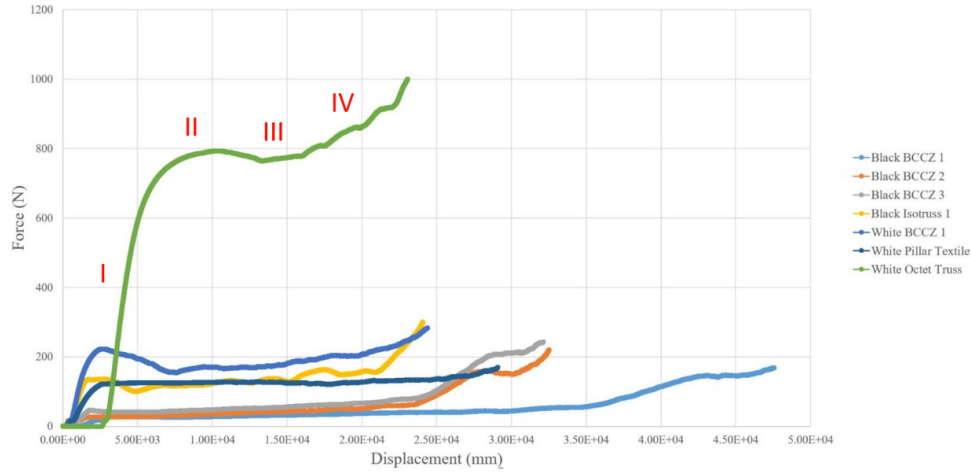


FIGURE 4.9: Load-Extension curves of the various microlattice geometries and materials tested.

TABLE 4.5: Summary of Lattice properties calculated from mechanical testing for lattice printed with black HDDA.

Sample	Stiffness (MPa)	Yield Strength (KPa)	Density (g/cc)	Specific Stiffness ($m^2s^{-2} \times 10^6$)	Rebound (%)
Black BCCZ 1	3.33	55	0.155	21.54	91.89
Black BCCZ 2	1.90	67.54	0.158	12.05	92.61
Black BCCZ 3	2.78	116.35	0.162	17.22	89.88
Black Isotruss	14.00	347.0	0.210	66.63	97.9

TABLE 4.6: Summary of Lattice properties calculated from mechanical testing for lattices printed with white HDDA.

Sample	Stiffness (MPa)	Yield Strength (KPa)	Density (g/cc)	Specific Stiffness ($m^2s^{-2} \times 10^6$)	Rebound (%)
White BCCZ	17.52	375.75	0.254	68.94	94.5
White Pillar Tex	7.99	317.5	0.202	39.58	95.47
White Octet Truss	34.817	792.92	0.394	88.33	93.2

Testing of the microlattices revealed that the octet truss lattice had the highest specific stiffness out of all the geometries. Figure 4.10 shows that similar to how some of the tensile bars failed, shear planes were obvious at 45degrees from the direction of loading. The lattices' mechanical response matched with that of theoretical stretch dominated lattices. As shown in Figure 4.9, lattices first experienced a region of elasticity (I), followed by a maximum stress after which where members begin to buckle(II), then a region of plastic collapse(III), and finally, full densification (IV) when the lattice becomes fully compressed. After being compressed well over 60% strain, many of the the struts had already buckled and broke off. Despite the irreversible damage done to the lattices, on average they returned to 93.6% of their original height. This is an interesting phenomena and could habve potential in the field of multi-impact energy management.

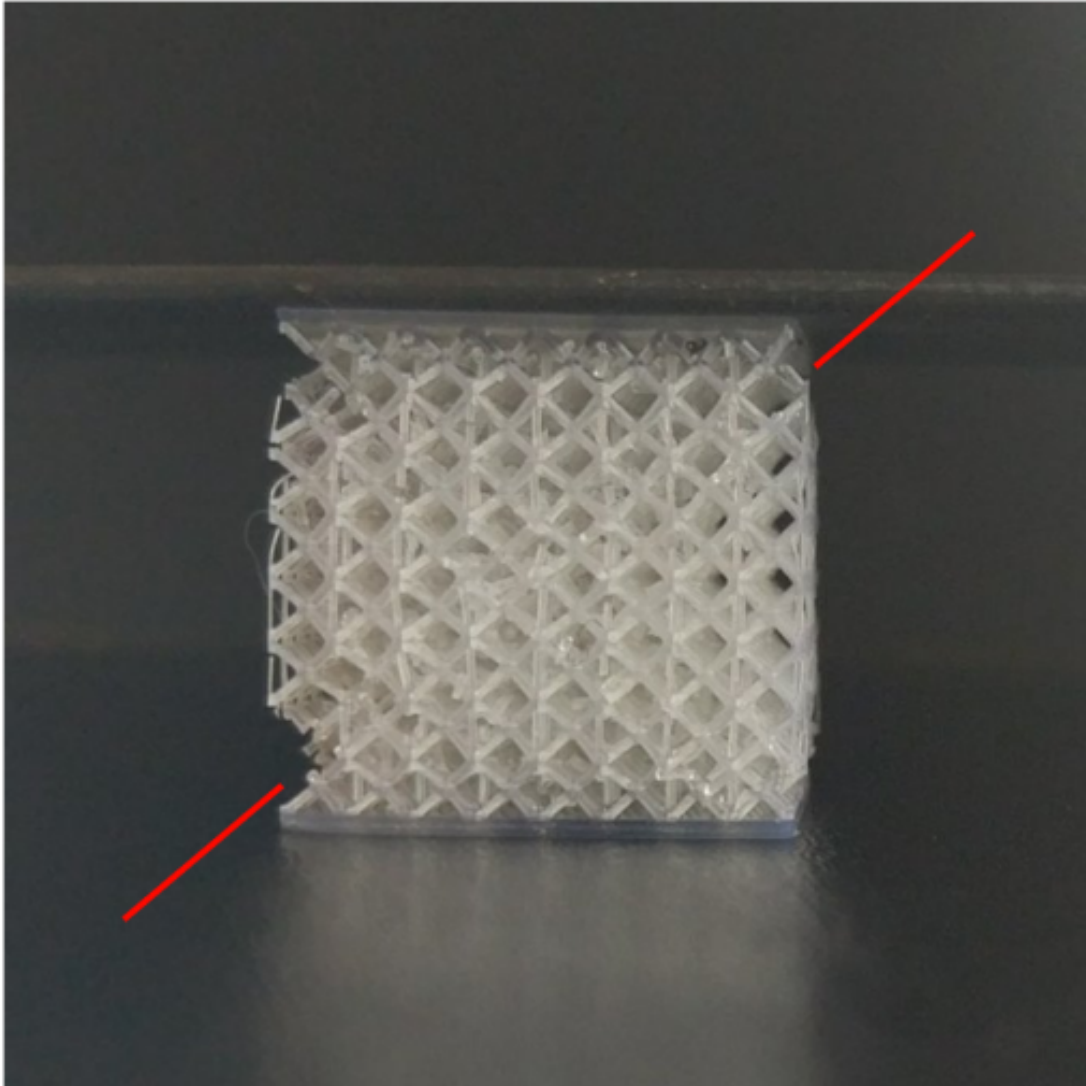


FIGURE 4.10: *A shear plane is visible along the red line on the BCCZ lattice.*

Chapter 5

Conclusions

This goal of this project was to obtain baseline data and mechanical property for Cal Poly's 316L stainless steel. This would allow students to design functional parts with proven strength values and make improvements to the printing process. Additionally, the compressive stiffness of 3D printed microlattices, a technology enabled by the SLM printing process, was investigated.

Mechanical properties of the heat treated, SLM printed stainless steel were tested in tension according to ASTM E8 specification. The microstructure and fracture surface of the material were examined using SEM imaging. Porosity and hardness tests were carried out and XRD analysis was employed for phase identification. Finally, four microlattice geometries were printed and tested in compression to determine which geometry had the highest specific stiffness.

- Mechanical properties of the heat treated 316L printed material are now established with the SLM printer at Cal Poly and parts can be designed with confidence.
- Yield strength and elongation (375.87 MPa and 32.45%, respectively) of Cal Poly's heat treated 316L stainless steel are slightly lower than other published values for as-printed 316L stainless. Young's modulus of the Cal Poly material was higher than other reported value.
- Post Processing is needed to achieve better surface finish, this is due to powder particles that are partially melted on the surface.
- Porosity of the material varies depending on many factors, Cal Poly's printed 316L stainless steel has below 1%.
- Microstructure of the as-printed 316L stainless has a refined, cellular dendritic microstructure due to the presence of δ -ferrite.
- Grains are preferentially aligned in both the as-printed and heat treated state as indicated by XRD analysis.
- There is evidence of δ -ferrite in both the heat treated and non-heat treated material indicated by XRD analysis and the use of a magnet.
- Ductile fracture is evident due to presence of shear lips, necking and dimples seen in SEM imaging.
- All other microlattice parameters being equal, the octet truss showed the highest strength and stiffness to weight ratio in compression.
- Lattices in compression showed typical stretch dominated behavior.

Chapter 6

Future Work

More characterization of 316L stainless steel could be done:

- Testing the mechanical properties of the as-printed material (without heat treatment).
- Testing the bars without machining the surface.
- Testing material anisotropy by printing bars at 90° and 45° from the build plate.
- Optimizing processing parameters to reduce warp, reduce porosity and increase mechanical properties.
- For the microlattices, different unit cell/strut diameter.

References

- [1] U. N. Gandhi, R. M. Gorguluarslan, Y. Song, and R. Mandapati, “Designing Lattice Structures For 3D Printing.”
- [2] V. Deshpande, N. Fleck, and M. Ashby, “Effective properties of the octet-truss lattice material,” *Journal of the Mechanics and Physics of Solids*, vol. 49, no. 1747-1769, 2001.
- [3] M. Santorinaios, W. Brooks, C. J. Sutcliffe, and R. Mines, “Crush behaviour of open cellular lattice structures manufactured using selective laser melting,” *WIT Transactions on The Built Environment.*, vol. 85, no. 481-489, 2006.
- [4] S. Tsopanos, R. Mines, Y.Chen, S. Mckown, W. Cantwell, and W. Brooks, “The Influence of Processing Parameters on the Mechanical Properties of Selectively Laser Melted Stainless Steel Microlattice Structures,” *Journal of Manufacturing Science and Engineering.*, vol. 132, 2010.
- [5] R. Gümruk, R. Mines, and S. Karadeniz, “Static mechanical behaviours of stainless steel microlattice structures under different loading conditions,” *Materials Science and Engineering*, vol. 586, no. 382-406, 2013.
- [6] N. Contuzzi, S. L. Campanelli, C. Casavola, and L. Lamberti, “Manufacturing and Characterization of 18Ni Marage 300 Lattice Components by Selective Laser Melting,” *Materials*, vol. 3, no. 3451-3468, 2013.
- [7] M. C. Messner, “Optimal lattice-structured materials,” *Journal of the Mechanics and Physics of Solids*, vol. 96, no. 162-183, 2016.
- [8] W. J. Sames, F. A. List, S. Pannala, R. R. Dehoff, and S. S. Babu, “The metallurgy and processing science of metal additive manufacturing,” *International Materials Reviews*, vol. 61, no. 5, 2016.
- [9] Z. Sun, X. Tan, S. B. Tor, and W. Y. Yeong, “Selective laser melting of stainless steel 316L with low porosity and high build rates,” *Materials and Design*, vol. 104, no. 197-204, 2016.
- [10] M. Seifi, A. Salem, J. B. Harrysson, and J. J. Lewandowski, “Overview of Materials Qualification Needs for Metal Additive Manufacturing,” *Journal of Materials*, vol. 66, no. 747-764, 2016.

- [11] M. L. M. Sistiaga, S. Nardone, C. Hautfenne, and J. V. Humbeeck, “Effect of Heat Treatment of 316L Stainless Steel produced by Selective Laser Melting.,” *27th Annual Solid Freeform Fabrication Symposium*, 2016.
- [12] D. Kianersi, A. Mostafaei, and A. A. Amadeh, “Resistance spot welding joints of AISI 316L austenitic stainless steel sheets: Phase transformations, mechanical properties and microstructure characterizations.,” *Journal of Materials and Design*, vol. 61, no. 251-263, 2014.